Chapter 5: Multimode Analysis of Periodic Dielectric Loaded Gyro-twystron Amplifier*

5.1 Introduction

5.2 Analytical Model

5.3 Coupler and RF Window

    5.3.1 Design and Simulation of the Input Coupler

    5.3.2 Design and Simulation of RF Window

5.4 RF Interaction Structure

    5.4.1 Modelling and Cold Simulation

    5.4.2 Hot Simulation Results

5.5 Parametric Analysis and Validation

5.6 Conclusion

5.1   Introduction

In the previous chapter (chapter 4), PDL gyro-twystron has been designed to suppress the second harmonic TE_{02} mode, which was identified as the most troublesome mode. In the present chapter, a multimode study of PDL gyro-twystron has been made to investigate the behaviour of operating and BWO modes in PDL waveguide section. The growth of operating TE_{01} mode as well as the suppression of TE_{02} is investigated using the nonlinear theory and PIC simulation. Recently, a multimode steady-state theory for gyro-TWT was developed to study its beam-wave interaction using both unloaded/smooth wall [91] and dielectric-loaded waveguide [107].

In the present chapter, the analytical model of the multimode theory is discussed in section 5.2. Design and simulation of subassemblies such as coupler and RF window is discussed in section 5.3. In section 5.4, the 3-D beam-wave interaction behaviour is discussed with vast simulation results. Parametric analysis of gyro-twystron has been done rigorously to optimize the performance and identify the operating limits in section 5.5. The analytical developments and predictions are validated by the 3-D PIC code CST particle studio. Findings of the present chapter are discussed in section 5.6.

5.2   Analytical model

A self-consistent nonlinear multimode model of PDL gyro-twystron has been developed to study its beam-wave interaction behaviour. This model helps to study the growth of desired operating mode and the suppression of parasites. In hybrid RF, structures the electrons get perturbed from the input cavity and ballistically bunched in the drift tube. Multimode formalism of cavity and drift tube remain same as discussed for the unloaded gyro-twystron in chapter 2 as the periodic dielectric loading is introduced in output waveguide section of gyro-twystron. The nonlinear interaction between the pre-bunched

electron beam and RF wave takes place in the PDL waveguide. In order to develop the multimode formalism, the following assumptions are incorporated [42], (i) Undisturbed mode distribution, i.e. in cylindrical waveguide the transverse field distribution remain same as it is in beam absent condition, and (ii) space charge effect is neglected. The lossy dielectric-loaded cylindrical waveguide is primarily divided into two regions as shown in figure 5.1. Region I $(0 < r < r_{dl}; 0 < z < L)$ is the vacuum region and region II is the lossy dielectric loaded region $(r_{dl} < r < r_w; 0 < z < w_d)$ [42], [108]. In Region, I, the axial magnetic and transverse electric fields for q number of modes are given by [42], [91]

$$H_{z\_I} = \sum_q F_q \; z \; \psi_{tq\_I} \; r,\varphi \; e^{j\omega_q t} \tag{5.1}$$

$$E_{t\_I} = \sum_q F_q \; z \; \frac{j\omega_q \mu}{k_{q\_I}^2 - k_{zq\_I}^2} \left[\vec{e}_z \times \nabla_t \psi_{tq\_I} \; r,\varphi \; \right] e^{j\omega_q t} \tag{5.2}$$

where, $F_q \; z$ is the field variation over the axial length (z), k_q is the total wave number of qth mode, k_{zq} is the axial wave number of qth mode and $\psi_{tq\_I} \; r,\varphi$ is the transverse field distribution in the region I, which is given as [42], [91]

$$\psi_{tq\_I} \; r,\varphi \; = J_{m_q} \; k_{tq\_I}r \; e^{-m_q\varphi} \tag{5.3}$$

Similarly, in region II the axial magnetic and transverse electric fields for q number of modes are given as,

$$H_{z\_II} = \sum_q F_q \; z \; \psi_{tq\_II} \; r,\varphi \; e^{j\omega_q t} \tag{5.4}$$

$$E_{t\_II} = \sum_q F_q \; z \; \frac{j\omega_q \mu}{k_{q\_II}^2 - k_{zq\_II}^2} \left[\vec{e}_z \times \nabla_t \psi_{tq\_II} \; r,\varphi \; \right] e^{j\omega_q t} \tag{5.5}$$

where, $\psi_{tq\_II} \; r,\varphi$ is the transverse field distribution in region II, which is given by,

$$\psi_{tq\_II} \; r,\varphi \; = C_1 J_{m_q} (k_{tq\_II}r) + C_2 N_{m_q} (k_{tq\_II}r)e^{-m_q\varphi} \tag{5.6}$$

The constants C_1 and C_2 are defined as,

$$C_1 = \frac{J_m(k_{tq\_I} r_{dl}) N'_m(k_{tq\_II} r_w)}{J_m(k_{tq\_II} r_{dl}) N'_m(k_{tq\_II} r_w) - J'_m(k_{tq\_II} r_{dl}) N_m(k_{tq\_II} r_w)}$$

$$C_2 = \frac{-J_m(k_{tI_q} r_{dl}) J'_m(k_{tq\_II} r_w)}{J_m(k_{tq\_II} r_{dl}) N'_m(k_{tq\_II} r_w) - J'_m(k_{tq\_II} r_{dl}) N_m(k_{tq\_II} r_w)}$$

The transverse electric field and the source current density are related for q number of modes as [42], [91],

$$\sum_q \left(\nabla_\perp^2 + \frac{\partial^2}{\partial z^2} + k_q^2 \right) \vec{E}_{tq} = \sum_q j\omega_q \mu \vec{J}_t \tag{5.7}$$

In a cylindrical waveguide, the electric field follows the uniform transverse distribution as in beam absent condition, which is given as,

$$\sum_q \nabla_t^2 \vec{E}_{tq} + \left[k_q^2 - k_{zq}^2 \right] \vec{E}_{tq} = 0 \tag{5.8}$$

Using the equation (5.5) in (5.4), we get,

$$\sum_q \left(\frac{\partial^2}{\partial z^2} + k_{zq}^2 \right) \vec{E}_t = \sum_q j\omega_q \mu \vec{J}_t \tag{5.9}$$

The wave equation (5.9) is perturbed by multiplying it on both sides with $\frac{\omega_q}{2\pi} \int_0^{2\pi/\omega_q} dt \int_{SI+SII} \int E_{tq}^* / F_q^* ds$, and the LHS is deduced into,

$$\sum_q \left(\frac{\partial^2}{\partial z^2} + k_{zq}^2 \right) F_q[z] G = \sum_q 2 j\omega_q \mu \vec{J}_t \int_{SI+SII} \int E_{tq}^* / F_q^* [z] ds \left(\frac{\omega_q}{2\pi} \right) \int_0^{2\pi/\omega_q} dt \tag{5.10}$$
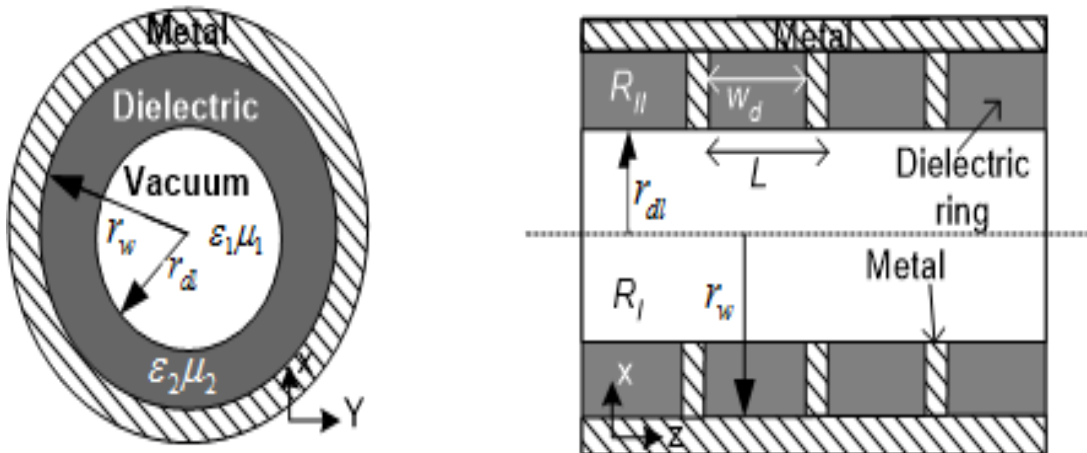

Figure 5.1 The transverse and longitudinal view of PDL waveguide

where,

$$G_q = \int_{SI} \int \left| \frac{j\omega_q \mu}{k_{q\_I}^2 - k_{kzq}^2} \left[\vec{e}_z \times \nabla_t \, \psi_{tq\_I} \quad r, \varphi \quad \right] \right|^2 ds + \int_{SII} \int \left| \frac{j\omega_q \mu}{k_{q\_II}^2 - k_{kzq}^2} \left[\vec{e}_z \times \nabla_t \, \psi_{tq\_II} \quad r, \varphi \quad \right] \right|^2 ds$$

$$\text{and } G = \sum_q G_q$$

By taking the curl of transverse field distribution and integrating it over the radial component, we are getting the geometric factor (G_{mn}), which is given by [35],

$$G_{mn} = \sum_q G_{m_q n_q} \text{ Where, } G_{m_q n_q} = K_{aq} + K_{bq}$$

$$G_{m_q n_q} = \frac{2\pi}{\left| k_{\perp q\_1}^2 \right|^2} \int_0^{r_{dl}} \left[\left| J'_{m_q}(k_{\perp q\_I} r) \right|^2 + \left| \frac{m}{k_{\perp 1_q} r} J_m(k_{\perp q\_I} r) \right|^2 \right] r \, dr + \frac{2\pi}{\left| k_{\perp q\_II}^2 \right|^2}$$

$$\int_{r_{dl}}^{r_w} \left\{ \left| \left[C_1 J'_m(k_{\perp q\_II} r) + C_2 N'_m(k_{\perp q\_II} r) \right] \right|^2 + \left| \frac{m}{k_{\perp q\_II} r} \left[C_1 J_m(k_{\perp q\_II} r) + C_2 N_m(k_{\perp q\_II} r) \right] \right|^2 \right\} r \, dr$$

The field amplitude (F) variation over the axial length (z) of lossy dielectric-loaded output waveguide inducing q modes with expanded current density in terms of electron distribution is given as,

$$\left(\frac{d^2}{dz^2} + k_{zq}^2 \right) F_q \quad z \quad = -\frac{2|I_b|}{G_{mn}} \sum_{i=1}^N W_i \frac{\beta_{ti}}{\beta_{zi}} \left[\frac{1}{k_{tq\_1}} J'_{s_q} \quad k_{tq\_1} r_{Li} \quad J_{m_q-s_q} \quad k_{tq\_1} r_{gi} \quad e^{-j\Lambda_i} \right] \quad (5.11)$$

The total phase distribution is expressed as $\Lambda = \omega_q t - s_q \theta - m_q - s_q \phi$, where, θ is the angle of electron position, ϕ is the guiding centre angle, k_z is the axial wave number, k_t is the transverse wave number, r_L is the Larmor radius, r_g is the beam radius and W_i is the weighing factor, which is expressed as, $\sum_{i=1}^{Ne} W_i = 1$, where N_e is the total number of electron. The axial velocity spread is modelled as a Gaussian distribution, which is expressed as $W_i = Ae^{-\left[p_{zi} - \bar{p}_z \, ^2 / 2\Delta p_z^2 \right]}$. In a PDL waveguide, the majority of EM power is

propagating through the unloaded region [35]. Therefore, the geometric factor (G_{mn}) is deduced into K_a, which is given as,

$$\left(\frac{d^2}{dz^2}+k_{zq}^2\right)F_q\ z\ =\frac{2|I_b|k_{tq\_1}}{\pi r_w^2 C_q}\sum_{i=1}^{Ne}W_i\frac{\beta_{ti}}{\beta_{zi}}\Big[J_{s_q}'\ k_{tq\_1}r_{Li}\ J_{m_q-s_q}\ k_{tq\_1}r_{gi}\ e^{-j\Lambda_i}\Big] \quad (5.12)$$

where, $C_q=\ x_{m_q n_q}^2-m_q^2\ J_{m_q}^2\ x_{m_q n_q}^2\ \Big/ x_{m_q n_q}^2$, n is the radial variation index of TE_{mn} mode, and x_{mn} is the Eigenvalue of TE_{mn} mode. The electron dynamics in the presence of applied electric and magnetic field is governed by Lorentz force equation [42],[91]

$$\frac{dp}{dt}=-e\ E+v\times B\ -e\vec{v}\times\ B_o\hat{z}\ +e\left(v\times\left(\frac{dB_o}{2dz}\right)\hat{r}\right) \quad (5.13)$$

The beam-wave interaction mechanism is governed by the set of coupled field equations which are representing the axial and transverse momenta, angle of electron position, gyrating radius and angle, respectively [42],[91]

$$\frac{dp_z}{dz}=-m_e c\frac{1}{2B_0}\frac{dB}{dz}\alpha\beta_t+e\mu\alpha\,\mathrm{Re}\left\{\sum_q\frac{1}{k_{tq\_1}}\begin{pmatrix}F_q'\ z\ J_{s_q}'\ k_{tq\_1}r_L\\ J_{m_q-s_q}\ k_{tq\_1}r_g\ e^{-j(s_q\theta+\ m_q-s_q\ \phi-\omega_q t)}\end{pmatrix}\right\} \quad (5.14)$$

$$\frac{dp_t}{dz}=m_e c\frac{1}{2B_0}\frac{dB}{dz}\beta_t-\frac{e\mu}{c\beta_z}\,\mathrm{Re}\left\{\sum_q\frac{1}{k_{tq\_1}}\begin{pmatrix}j\omega_q F_q\ z\ +c\beta_z F_q'\ z\ J_{s_q}'\ k_{tq\_1}r_L\\ J_{m_q-s_q}\ k_{tq\_1}r_g\ e^{-j(s_q\theta+\ m_q-s_q\ \phi-\omega_q t)}\end{pmatrix}\right\} \quad (5.15)$$

$$\frac{d\theta}{dz}=\frac{eB_0}{p_z}-\frac{e\mu}{c\beta_z p_z}\,\mathrm{Re}\left\{\sum_q\frac{1}{k_{tq\_1}^2}\begin{pmatrix}\left(\dfrac{s_q\omega_q}{r_L}F_q\ z\ -\dfrac{\beta_t k_{tq\_1}^2}{c}F_q\ z\ -\dfrac{js_q\beta_z}{r_L c}F_q'\ z\right)\\ J_{s_q}\ k_{tq\_1}r_L\ J_{m_q-s_q}\ k_{tq\_1}r_g\ e^{-j(s_q\theta+\ m_q-s_q\ \phi-\omega_q t)}\end{pmatrix}\right\} \quad (5.16)$$

$$\frac{dr_g}{dz}=-\frac{1}{2B_0}\frac{dB}{dz}r_g+\frac{\mu}{c\beta_z B_0}$$

$$\left\{\begin{array}{l}\dfrac{1}{k_{tq\_1}^2}\ J_{s_q}'\ k_{tq\_1}r_L\ J_{m_q-s_q}\ k_{tq\_1}r_g\ \mathrm{Re}\ j\omega_q F_q\ z\ +c\beta_z F_q'\ z\ e^{-j(s_q\theta+\ m_q-s_q\ \phi-\omega_q t)}\\ \sum_q\ -\begin{pmatrix}J_{s_q-1}\ k_{tq\_1}r_L\ J_{m_q-s_q+1}\ k_{tq\_1}r_g\\ -\ J_{s_q+1}\ k_{tq\_1}r_L\ J_{m_q-s_q-1}\ k_{tq\_1}r_g\end{pmatrix}\mathrm{Im}\left(\dfrac{1}{2}F_q\ z\right)e^{-j(s_q\theta+\ m_q-s_q\ \phi-\omega_q t)}\end{array}\right\} \quad (5.17)$$

$$\frac{d\phi}{dz} = \frac{\mu}{c\beta_z B_0}$$

$$\left\{ \sum_q \begin{array}{c} \frac{1}{k_{\perp q\_1}^2} \frac{m_q - s_q}{r_b} \; J_{s_q}\left(k_{\perp q\_I} r_L\right) \; J_{m_q-s_q}\left(k_{\perp q\_I} r_g\right) \; \mathrm{Im}\left[\left(j\omega_q F_q(z) + c\beta_z F_q'(z)\right) e^{j\varphi}\right] \\ -\left(\begin{array}{c} J_{s_q-1}\left(k_{\perp q\_I} r_L\right) J_{m_q-s_q+1}\left(k_{\perp q\_I} r_g\right) + \\ J_{s_q+1}\left(k_{\perp q\_I} r_L\right) J_{m_q-s_q-1}\left(k_{\perp q\_I} r_g\right) \end{array} \right) \mathrm{Re}\left(\frac{1}{2} F_q(z)\right) e^{-j\left(s_q\theta + (m_q-s_q)\phi - \omega_q t\right)} \end{array} \right\} \quad (5.18)$$

Based on the stability analysis of gyro-twystron [109], the present PDL waveguide (figure 5.1) is designed and studied for its multimode behaviour. The main objective of introducing lossy dielectric loading is to suppress the backward wave oscillations (BWOs) including TE_{11}, TE_{21}, and second harmonic TE_{02} modes that are vulnerable to the stability of the device. The growth of field associated with the desired operating TE_{01} and the spurious second harmonic TE_{02} modes along the PDL waveguide is shown in Figure 5.2. This clearly shows that the desired mode is grown in the unloaded nonlinear section of RF circuit and all other BWOs are significantly suppressed. The present design predicted a significant RF power of ~26 MW at 10 GHz in TE_{01} mode (Figure 5.3). However, the multi-mode code also predicted the power shared by other spurious BWOs

Table 5.1 Structural parameters of PDL gyro-twystron

| Particulars	Values
Beam Voltage	440 kV
Beam Current	220 A
Beam-velocity pitch factor	1.0
Velocity spread	4%
Pre-drift section length	32 mm
Input cavity radius	28.1 mm
Input cavity length	17.3 mm
Drift section radius	15 mm
Drift section length	143.6 mm
Waveguide radius	19.5 mm
Unloaded Waveguide length	130 mm
Loaded Waveguide length	120 mm
Guiding centre radius	0.4615 r_w
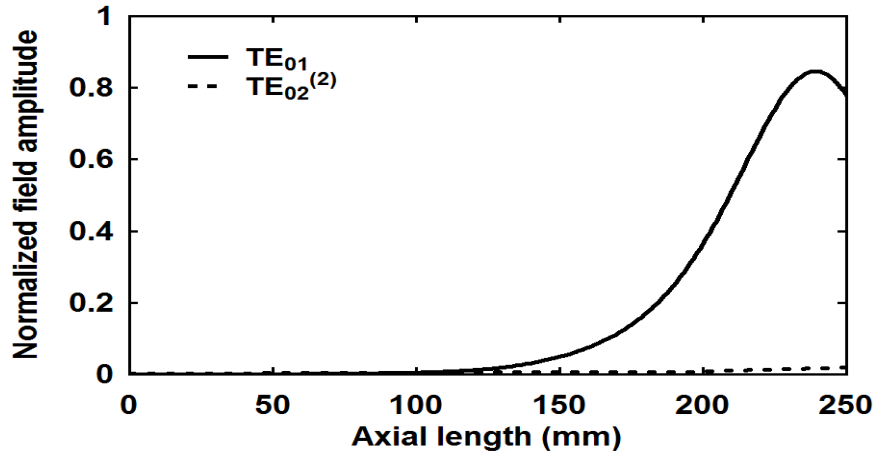
Figure 5.2 Field amplitude variation along the axial length of waveguide.
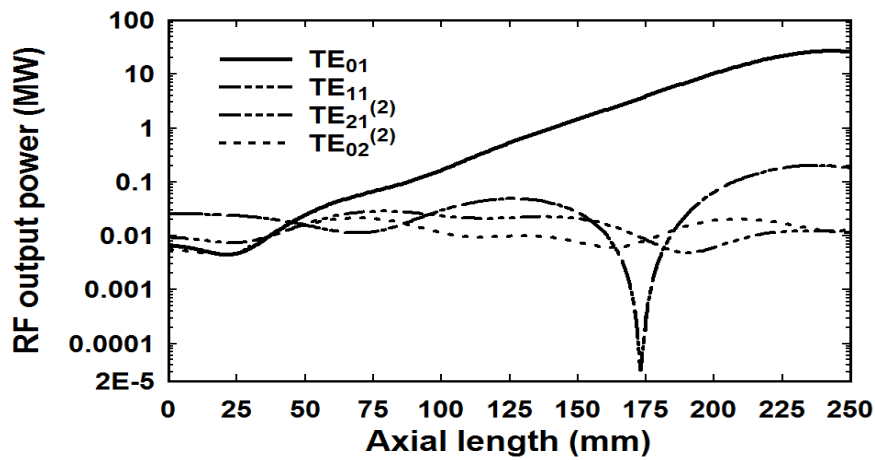

Figure 5.3 RF output power growth along the axial direction of the waveguide.

including TE_{11}, TE_{21} and second harmonic TE_{02} modes. It shows that only a meager amount of power in the range of few kW is shared by these BWOs (Figure 5.3), due to the mode suppression property of lossy dielectrics present in the RF section. This is evident that the PDL waveguide significantly suppressed the second harmonic TE_{02} mode along with the other BWOs, including TE_{11} and TE_{21} modes.

5.3 Coupler and RF window

5.3.1 Design and simulation of the Input coupler

The wraparound coupler is designed to feed the RF power to the input cavity with a higher degree of desired mode purity[110]. The input coupler should have high average power

operation and wide bandwidth with the minimum reflections. The RF structure of input coupler consists of a rectangular waveguide, coaxial cavity and inner input cavity as shown in figure 5.4 (a). The rectangular waveguide is operating in TE_{10} mode coupled to the coaxial cavity. The wide and narrow dimension of the rectangular cavity is chosen such that it supports the propagation of TE_{10} mode at operating frequency and TE_{10} mode coupled to the coaxial cavity. CST model with the E-field distribution is shown in figure 5.4 (b). The wide and narrow dimension of the rectangular waveguide is kept 21 mm and 10.5 mm, respectively. The inner radius (r_{in}) and outer radius (r_{out}) of the cavity is chosen such that coaxial cavity resonate in TE_{m11} mode at desired frequency [110] and the difference between the radii should not be larger than the narrow dimension of rectangular waveguide (*b*) [110]. To achieve the desired resonating frequency at TE_{m11}, an adjustment in the outer radius is preferred over inner radius due to a fixed inner cavity radius (r_{cav}) [110]. The outer and inner radii of the coaxial cavity are kept ~44.1 mm and ~33.6 mm, respectively. The design of input coupler follows the inequalities,

$$r_{out} - r_{in} < b \text{, and } L_{coax} \geq a .$$

Coupling slots(m) = Azimuthal index of resonating TE mode in the coaxial cavity
Azimuthal Spacing $_{\text{rectangular coupling slots}}$ = 360^0/m , (*m ≥3*),

The odd numbers of rectangular slots are chosen to reduce the excitation of TE_{21} mode in TE_{01} operated cavity. We have created the five rectangular slots, interspaced by 72^0 to one another. The ratio of optimised azimuthal width to optimized axial length of rectangular slots are kept half (0.5) [110]. For high power operation, the quality factor of the inner cavity is lowered by increasing the slot dimensions, and variation in axial length of the slot is preferred over the azimuthal length of slot [110]. For better results, the coaxial cavity and inner cavity are tuned at the same resonating frequency near 10 GHz. This complex structure is modelled by hexahedral meshing with perfect boundary

approximation, and cold analyzed in "CST Microwave Studio" [96]. The vector distribution of the electric field of TE_{10} mode in rectangular and the excitation of desired
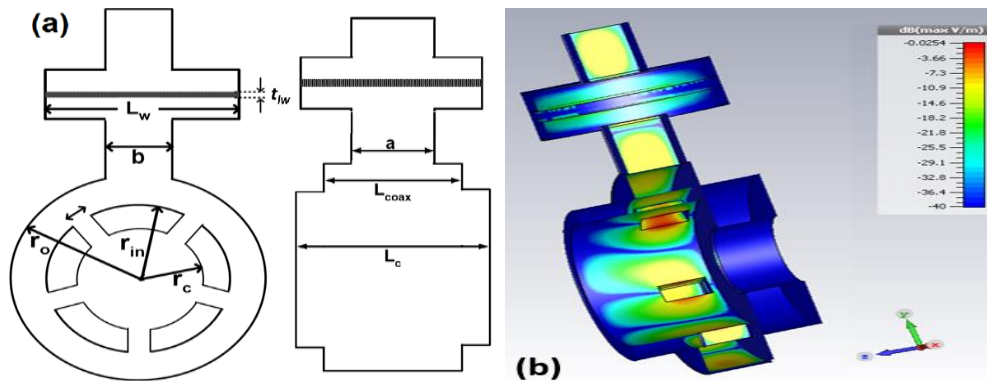

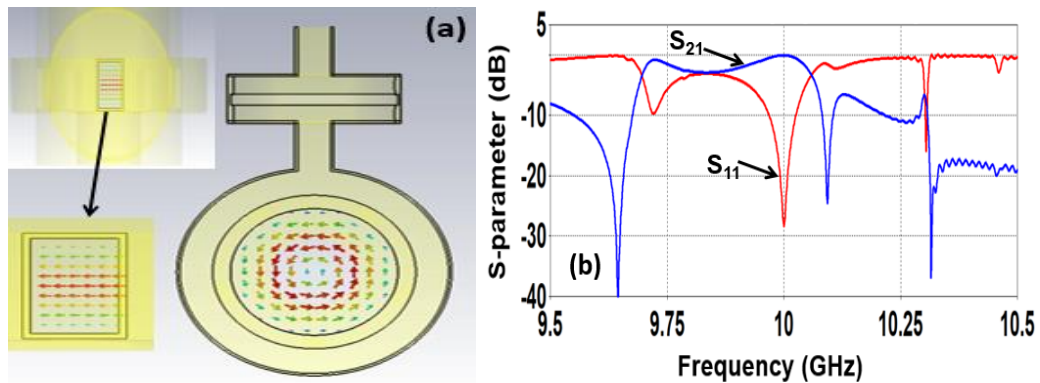Figure 5.4 (a) Schematic and (b) CST model of mode launcher with electric field distribution.

Figure 5.5 (a) Vector plot of TE_{10} mode (port 1) and TE_{01} mode (port 2) of the input coupler and (b) Scattering coefficients of the input coupler

Table 5.2 Structural parameters of input coupler

Input coupler	
Parameters	**Values**
Wide dimension of rectangular waveguide *(a)*	20 mm
The narrow dimension of rectangular waveguide *(b)*	10 mm
The outer radius of the Coaxial cavity *(r_o)*	45.1 mm
The inner radius of the Coaxial cavity *(r_{in})*	33.6 mm
Length of Coaxial cavity *(L_{coax})*	20 mm
Length of rectangular slots *(S_L)*	15 mm
Width of rectangular slots *(S_w)*	7.5 mm
The radius of the central cavity *(r_{cav})*	28.1 mm

Table 5.3 Structural parameters of RF window

Output RF window	
Parameters	**Values**
The thickness of the RF window *(t_w)*	4.83 mm
The Radius of the RF window (r_win)	64 mm
The relative permittivity of Window disc	9.6
The loss tangent of RF window	0.0003 (at 10 GHz)

TE_{01} mode in the central cavity are shown in Figure 5.5(a). The transmission (S_{21}) and return (S_{11}) losses of input coupler are computed as ~0.13 dB and ~28 dB, respectively at 10 GHz [Figure 5.5(b)]. The optimized design parameters of the RF input coupler are given in TABLE 5.2.

5.3.2 Design and simulation of RF window

The RF window isolates the inner vacuum region and external atmospheric pressure and provides the RF power transmission with minimum reflections. The RF window is designed to minimize the reflections for operating mode at the desired frequency. To achieve the zero reflectivity, the thickness *(t_w)* of RF window is chosen equal to the integer multiple of half-wavelength *(λ)* for corresponding operating frequency in the dielectric *(ε)* medium and expressed as [111],

$$t_w = N\lambda / 2\left(\sqrt{\varepsilon_{rw}}\right)$$

The material for RF window and its disk thickness are chosen to achieve high average power operation, and it should have sustainable mechanical strength. Alumina having a dielectric constant of 9.6 with the loss tangent of 0.003 at 10 GHz is chosen as RF window. Non-toxic alumina is having moderate thermal conductivity and good mechanical strength. From Figure 5.6 (a), it can be seen that the minimum reflectivity of

the RF window is achieved for the thickness of 4.83 mm at 10 GHz for N=1. The optimized design parameters of the RF window are given in TABLE 5.3. The present RF window is modelled with a circular dielectric disk having a radius of 64mm and thickness of 4.83 mm [Figure 5.6 (b)]. Figure 5.7 (a) shows the confinement of desired operating TE$_{01}$ mode at 10 GHz. The cold simulation of the present RF window predicted the transmission loss of 0.0075 dB and return loss of ~ 63 dB at 10 GHz [Figure 5.7 (b)].
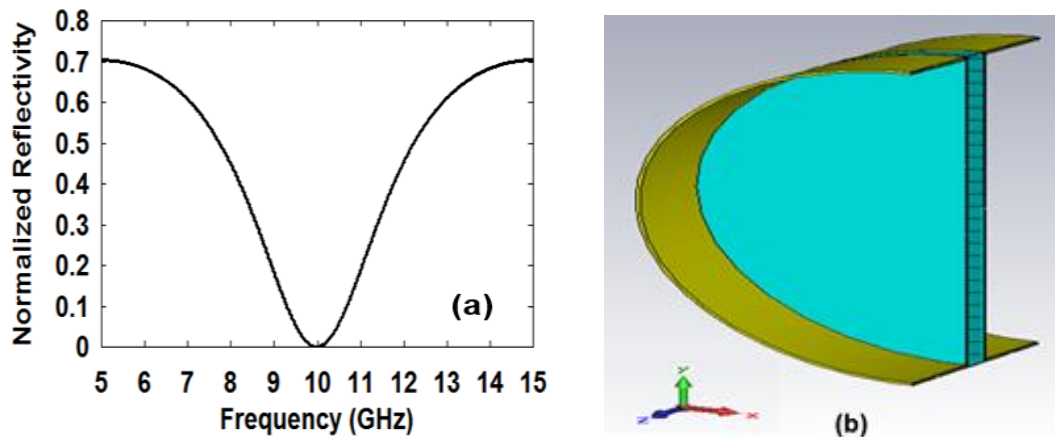
Figure 5.6 (a) Reflectivity of RF window Vs frequency and (b) its CST model
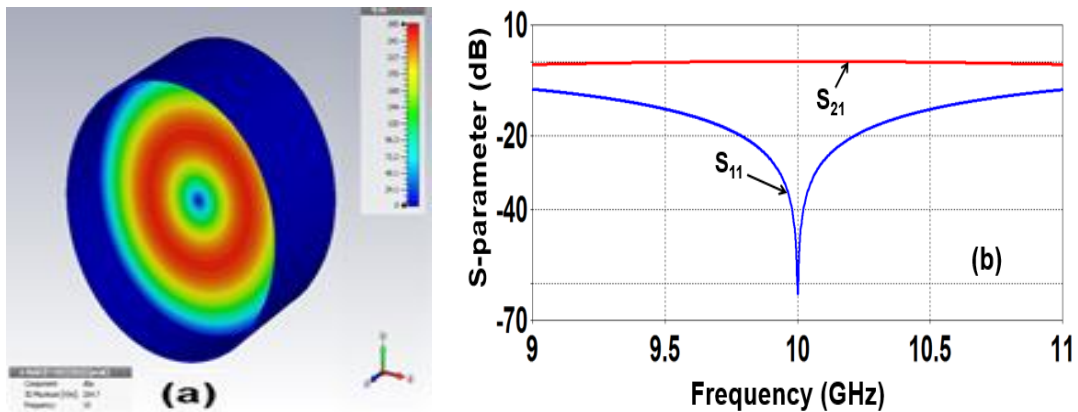
Figure 5.7(a) CST model and E-field distribution of TE$_{01}$ mode in RF window and (b) Scattering parameters of RF window

5.4 RF Interaction Structure

5.4.1 Modelling and Cold Simulation

RF interaction structure of gyro-twystron (Figure 5.8) is modelled in "CST Particle Studio" using structural parameters given in Table 5.1. The radius of the input cavity is 28.1 mm, and its length is 17.3 mm. The input cavity is loaded with dielectric rings at its

downstream to lower the quality factor to ~254. The cold analysis of the input cavity confirms the desired operating TE_{01} mode at 10 GHz (Figure 5.9). To provide an efficient bunching at the centre of the input cavity, a pre-drift length of ~32 mm is employed between the particle emitter and input cavity. This also avoids the backward wave propagation towards the electron gun. The radii of both pre-drift and drift tube are chosen as 15 mm to cut-off the operating TE_{01} mode. A lengthy 140 mm field-free drift tube is realized with three stacks of five tapered BeO-SiC rings that provide the isolation between the input cavity and output waveguide. The propagation characteristic (Figure 5.10) of heavily attenuating drift tube clearly indicates that the transmission loss of all considered TE modes is well above 50 dB, as required. At the end of the drift tube, a 20 mm length of the nonlinear taper is used to minimize reflections. This also acts a transition section between the drift tube of 15 mm radius and output waveguide radius of 19.5 mm. The main output waveguide length of 250 mm is modelled using stainless steel with a conductivity of 6.99×10^6 S /m and its background has been set as normal (vacuum). The waveguide is loaded periodically with lossy dielectric rings for the first 120 mm of its length. The lossy dielectric rings having the radial thickness of 1mm and axial thickness of 2 mm, which are inserted or fitted completely into metallic grooves. The lossy dielectric rings are spaced alternatively with 3 mm metal space between them.

1. Particle emitter 2. Predrift tube
3. Input cavity 4. Drift tube
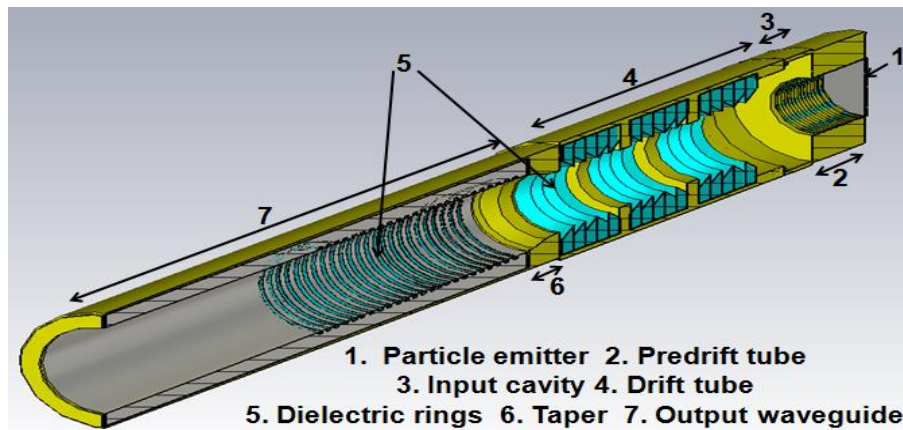5. Dielectric rings 6. Taper 7. Output waveguide

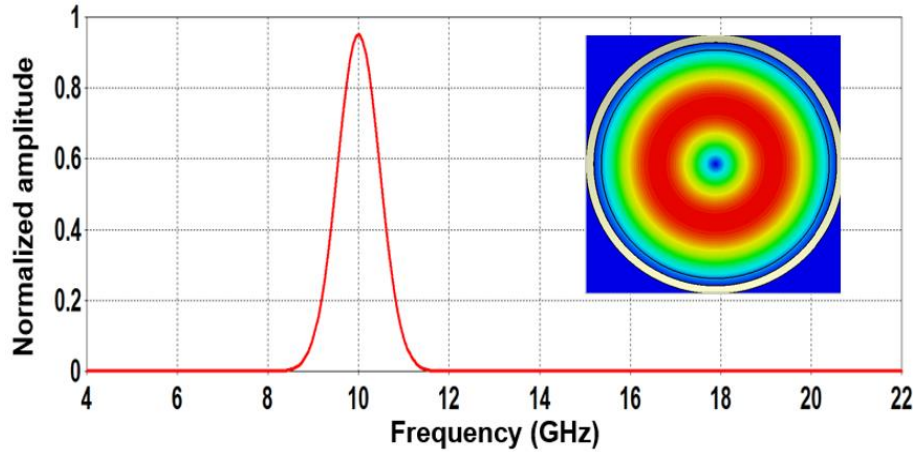Figure 5.8 Modeled gyro-twystron RF interaction circuit with particle emitter.

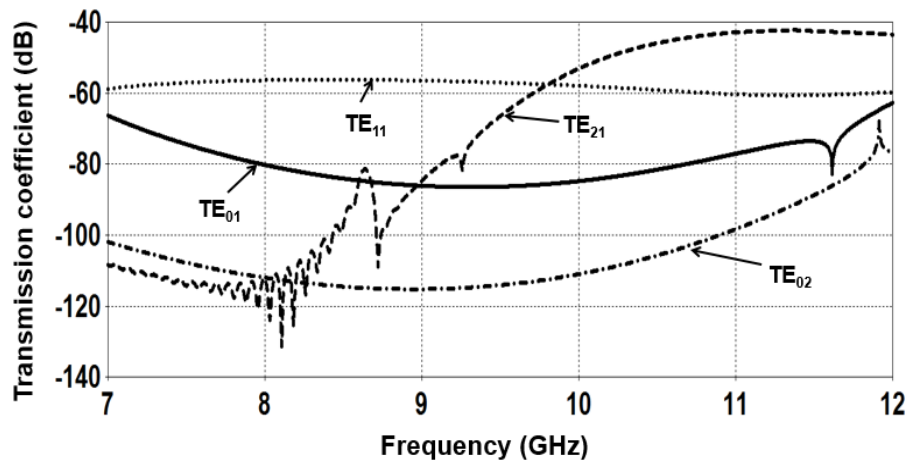Figure 5.9 Confinement of E-field at the resonant frequency of the input cavity.

Figure 5.10 Transmission loss on different modes in the drift tube.

5.4.2 Hot Simulation Results

3D beam-wave interaction behavior in a PDL gyro-twystron is studied using "CST Particle Studio" which accounts for multiple modes in the computation. The algorithm interpolates the discretized Maxwell's equations and particle dynamics equations for small-time step iteratively [96]. A thin circular disk of kinetic type DC emission model is used with the Lorentz factor (gamma) of 1.841. To maximize the beam-wave coupling, 40 emission points are defined with the guiding centre radius of 9mm and the beam-velocity pitch factor of one. The momentum and phase of electrons are perturbed by the RF input signal at the input cavity. This leads to ballistic bunching in drift space and results in pre-bunched electron beam at the entrance of output waveguide. At the wall of

the RF structure, the tangential electric field (E_t) is set as zero. The meshing technique is dividing the RF structure into the independent Cartesian coordinate system and creating a large number of small cells. The total number of mesh cell depends on cell per wavelength that ensures the minimum field sampling rate for EM computation with high accuracy. In the present simulation, the optimum cell per wavelength is defined as ten that results in the total number of mesh cells of ~8957760. Figure 5.11 shows the momentum or energy of electrons at a different position along the axial direction of the RF interaction structure during the beam-wave interaction process. Initially, all emitted electrons have the same energy of ~440 keV, and all beamlets have the same Larmor radii. Obviously, the applied RF input signal perturbs the homogeneity of helically moving particles that result in bunching of electrons. The non-homogeneity is due to the variation in Larmor radius and cyclotron frequency of electron. Once these bunched electrons slipped into the retarding phase, the transverse kinetic energy of electrons is transferred to EM field. The colour on the energy bar indicates the amount of energy or kinetic parameter of electrons during the interaction process. In the present simulation, 5,66,7100 particles are involved in the interaction process. At the end of the waveguide section, the energy of most particles is low that confirms the majority of electrons are lost their energy to RF wave. In the present study, a kinetic type electron beam is chosen with the spread of 4%, and its kinetic value is 0.843c. Figure 5.11 shows the normalized momentum of electrons that elucidates the beam wave interaction behaviour in the presence of magnetic field tapering. The momentum of particles is uniform with high energy during the beam-wave interaction and start decreasing after 230mm of RF interaction circuit (Figure 5.11). The decrease in momentum shows that some particles give up its transverse kinetic energy to the RF wave. The developed amplitude of ~5 k $\sqrt{W}$ (brown) in the desired TE$_{01}$ mode and 400k $\sqrt{W}$ (blue) in a closely competing for

second harmonic TE_{02} mode are shown in Figure 5.12. The corresponding RF output power in the desired TE_{01} mode is obtained ~25 MW (Figure 5.13). Figure 5.14 confirms the operating frequency of the device at 10 GHz corresponds to TE_{01} mode without any harmonic generation. Therefore, the lossy dielectric loading in gyro-twystron suppressed the second harmonic TE_{02} mode.
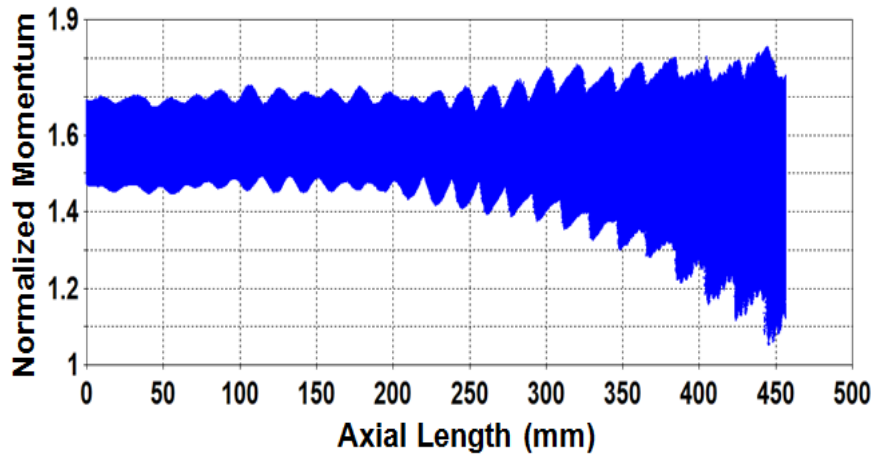

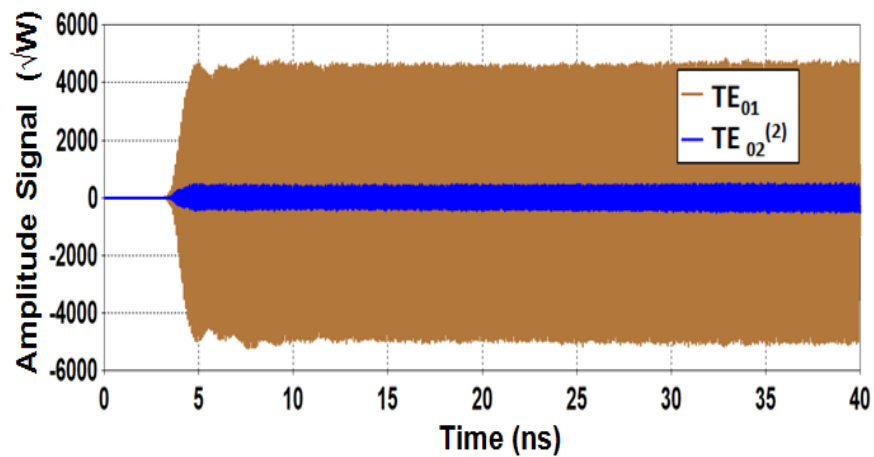Figure 5.11 Particles' normalized momentum variation over the axial length (with 4 % spread in particles velocity).

Figure 5.12 RF output signal amplitude developed in TE_{01} and TE_{02} modes (with the drive input power of 85 kW).
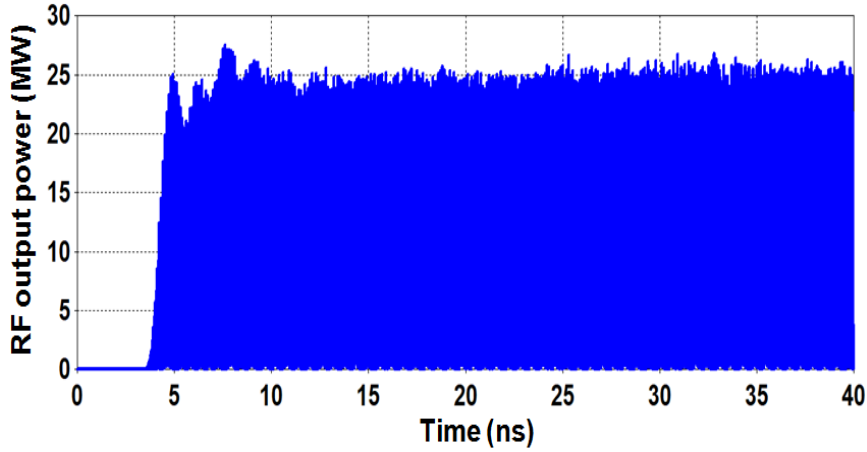
Figure 5.13 RF output power developed in TE_{01} mode monitored at the end of RF interaction structure (V_b=440 kV, I_b=220 A with 4% velocity spread).
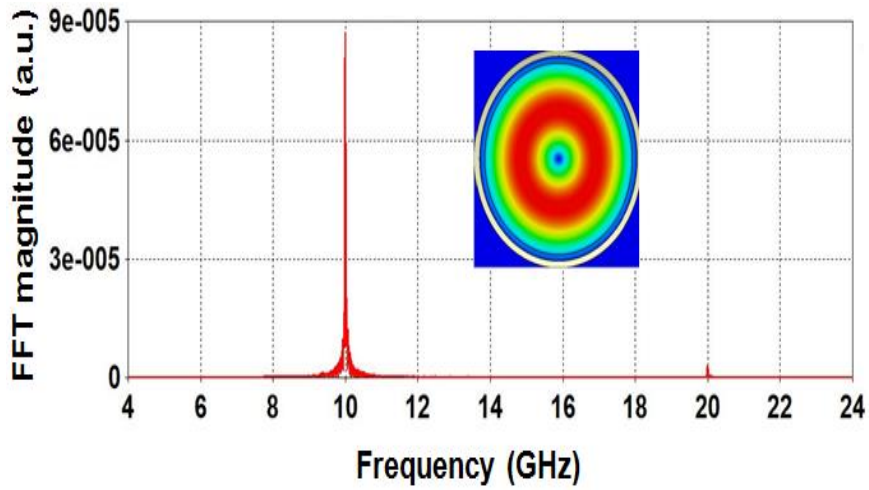

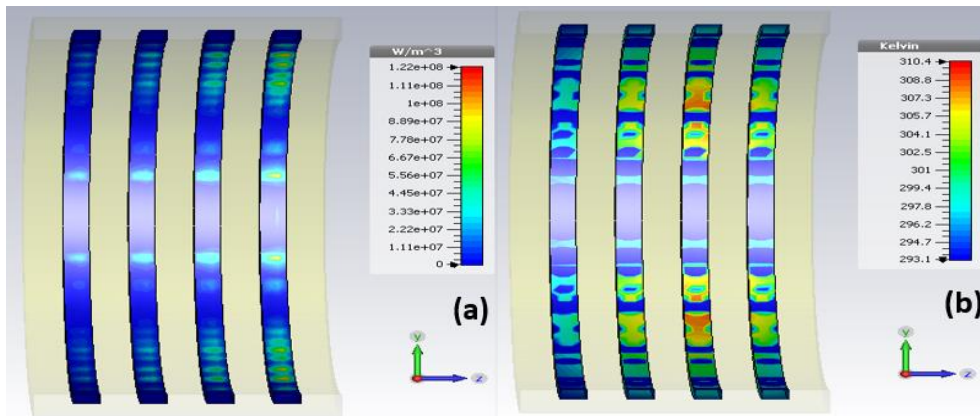Figure 5.14 Frequency spectrum of the output signal in TE_{01} mode.

Figure 5.15 Thermal loss distribution and (b) temperature rise in the last four BeO-SiC rings. (for fixed r_{th}=1 mm and w_d=2 mm)

Further, thermal loss and the corresponding temperature rise in the last four rings are calculated using transient thermal solver of CST Mphysics Studio [96]. The maximum developed RF power near 120 mm (where the last ring is placed) is 0.7 MW (shown in Figure 5.3), which is considered in the calculation of dissipation loss. The thermal loss distribution and corresponding temperature rise are shown in Figure 5.15 (a) and Figure 5.15 (b), respectively. It is observed from Figure 5.15(a) that the thermal volume loss is 122 MW /m³ (0.122 kW/cm³) in the last ring near 120 mm. The corresponding temperature rise is observed as ~310 K [Figure 5.15(b)].
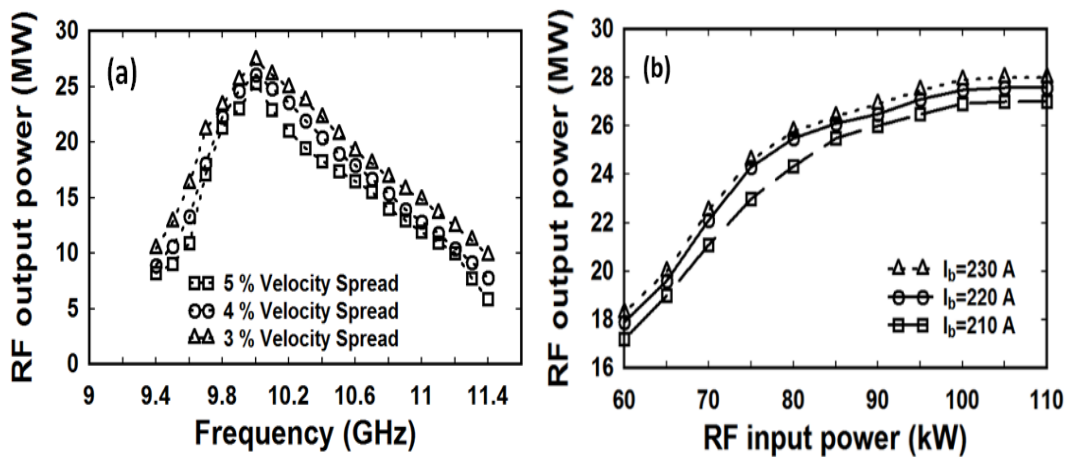

Figure 5.16 Variation of (a) saturated RF output power and (b) gain over the RF drive power (the beam voltage is fixed at 440 kV).
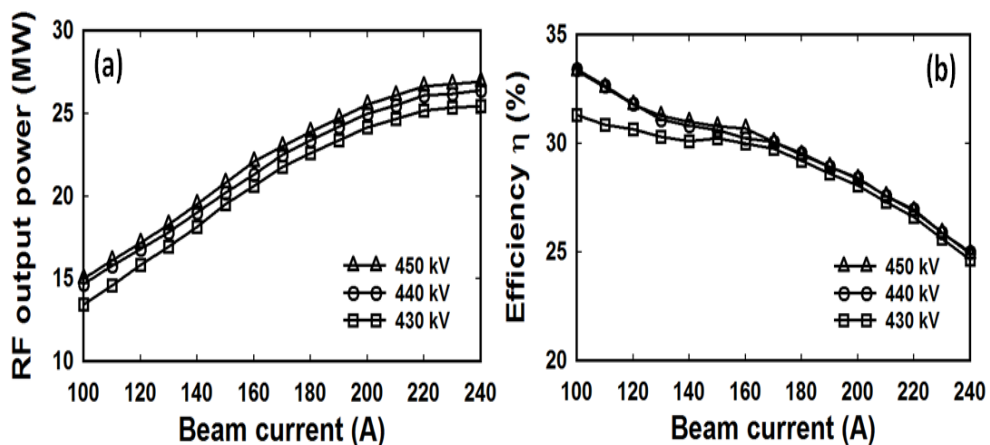

Figure 5.17 The variation of (a) RF output power (b) efficiency over the beam current (the drive input power is fixed at 85 kW).
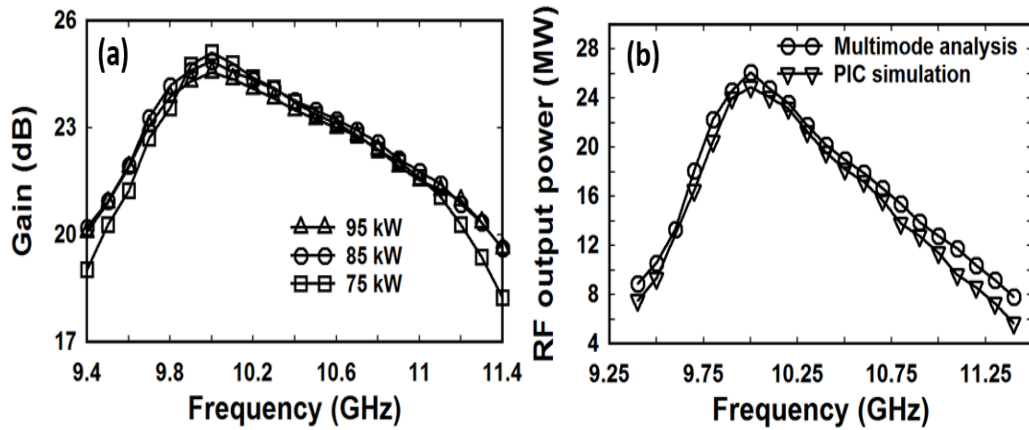
Figure 5.18 (a) Gain over the frequency for different RF drive power (b) Comparison of multimode and PIC simulation response of PDL gyro-twystron (V_b=440kV, I_b=220 A with unity beam velocity pitch factor and 4% velocity spread).

5.5   Parametric Analysis and Validation

To maximize the RF output power, gain, bandwidth, and efficiency various electrical parameters including RF input power, beam voltage, beam current have been optimized, while fixing the circuit parameters. The variation of RF output power over the frequency for different velocity spread is shown in Figure 5.16 (a). As the spread of electron increases, the output power decreases due to the limit on Doppler up-shift operation of gyro-twystron. A linear variation of output power with respect to input power is observed. However, the gain drops slightly above 75 kW of input drive [(Figure 5.16 (b)]. However, the amplifier is being saturated beyond 80kW with a maximum RF output power of ~26 MW and the corresponding gain of ~25 dB. The RF output power [Figure 5.17 (a)] and the corresponding gain [Figure 5.17 (b)] of amplifier remain constant at the operating frequency of 10GHz, for the input drive above 75 kW. For maximizing the RF power [Figure 5.17 (a)] and the corresponding electronic efficiency [Figure 5.17 (b)], the beam current is optimized while fixing the beam voltage. As the beam current increases, the output power also increases, but beyond 220 A, the output becomes saturated (Figure 5.17). Though the output power increases for higher beam voltages, the desired efficiency

of ~27 % is obtained for the DC values of 440 kV and 220-240 A. The present multimode response of the amplifier is validated through a 3D commercial PIC code (Figure 5.18).

5.6 Conclusion

An X-band PDL gyro-twystron has been studied for its beam wave interaction behavior using multimode theory. The use of lossy dielectric loading in the output non-resonant structure provides heavy attenuation to parasites including TE_{11}, TE_{21}, and second harmonic TE_{02} modes that result in the stable operation of the amplifier. The multimode analysis of gyro-twystron predicted a peak RF output power of ~26 MW in TE_{01} mode for the gyrating electron beam of 440 kV, 220 A, with a spread of 4 %. The conversion efficiency of PDL gyro-twystron has been calculated as ~27 % and the saturated gain as ~25 dB. The multimode results are found to be close in agreement with the 3D simulation of gyro-twystron by ~4 %. For further performance enhancement in gyro-twystron amplifier, an intermediate cavity is introduced which is discussed in next chapter.